Asian Journal of Pharmaceutical Sciences 17 (2022) 206–218

Available online at www.sciencedirect.com

ScienceDirect

journal homepage: www.elsevier.com/locate/AJPS

Original Research Paper

A pH-sensitive supramolecular nanosystem with chlorin e6 and triptolide co-delivery for chemo-photodynamic combination therapy

Yihan Wu[a,†], *Jingjing Li*[a,b,†], *Xuemei Zhong*[a], *Jinfeng Shi*[a], *Yanfen Cheng*[a], *Chenglin He*[a], *Jiaxin Li*[a], *Liang Zou*[c], *Chaomei Fu*[a], *Meiwan Chen*[d], *Jinming Zhang*[a,*], *Huile Gao*[e,*]

[a] *School of Pharmacy, Chengdu University of Traditional Chinese Medicine, Chengdu 611137, China*
[b] *Department of Pharmacology and Pharmacy, The University of Hong Kong, Hong Kong SAR, China*
[c] *School of Food and Biological Engineering, Chengdu University, Chengdu 610106, China*
[d] *Institute of Chinese Medical Sciences, University of Macau, Macau, China*
[e] *West China School of Pharmacy, Sichuan University, Chengdu 610041, China*

ARTICLE INFO

Article history:
Received 5 October 2021
Revised 23 November 2021
Accepted 13 December 2021
Available online 16 January 2022

Keywords:
Triptolide
Chemo-photodynamic
pH-sensitive supramolecular
Nanosystem
Co-delivery

ABSTRACT

The combination of Ce6, an acknowledged photosensitizer, and TPL, a natural anticancer agent, has been demonstrated as a useful strategy to reinforce the tumor growth suppression, as well as decrease the systemic side effects compared with their monotherapy. However, in view of the optimal chemo-photodynamic combination efficiency, there is still short of the feasible nanovehicle to steadily co-deliver Ce6 and TPL, and stimuli-responsively burst release drugs in tumor site. Herein, we described the synergistic antitumor performance of a pH-sensitive supramolecular nanosystem, mediated by the host–guest complexing between β-CD and acid pH-responsive amphiphilic co-polymer mPEG-PBAE-mPEG, showing the shell–core structural micelles with the tight β-CD layer coating. Both Ce6 and TPL were facilely co-loaded into the spherical supramolecular NPs (TPL+Ce6/NPs) by one-step nanoprecipitation method, with an ideal particle size (156.0 nm), acid pH-responsive drug release profile, and enhanced cellular internalization capacity. In view of the combination benefit of photodynamic therapy and chemotherapy, as well as co-encapsulation in the fabricated pH-sensitive supramolecular NPs, TPL+Ce6/NPs exhibited significant efficacy to suppress cellular proliferation, boost ROS level, lower MMP, and promote cellular apoptosis *in vitro*. Particularly, fluorescence imaging revealed that TPL+Ce6/NPs preferentially accumulated in the tumor tissue area, with higher intensity than that of free Ce6. As expected, upon 650-nm laser irradiation, TPL+Ce6/NPs exhibited a cascade of amplified synergistic chemo-photodynamic therapeutic benefits to suppress tumor progression in both hepatoma H22 tumor-bearing mice and B16 tumor-bearing mice. More importantly, lower systemic toxicity was found in the tumor-bearing mice treated with

* Corresponding author.
E-mail addresses: cdutcmzjm@126.com (J.M. Zhang), gaohuile@scu.edu.cn (H.L. Gao).
† These authors contributed equally to this paper
Peer review under responsibility of Shenyang Pharmaceutical University.

https://doi.org/10.1016/j.ajps.2021.12.003
1818-0876/© 2022 Shenyang Pharmaceutical University. Published by Elsevier B.V. This is an open access article under the CC BY-NC-ND license (http://creativecommons.org/licenses/by-nc-nd/4.0/)

TPL+Ce6/NPs. Overall, the designed supramolecular TPL+Ce6/NPs provided a promising alternative approach for chemo-photodynamic therapy in tumor treatment.

© 2022 Shenyang Pharmaceutical University. Published by Elsevier B.V.
This is an open access article under the CC BY-NC-ND license (http://creativecommons.org/licenses/by-nc-nd/4.0/)

1. Introduction

Bioactive natural products have become an indispensable source of modern medicines. TPL, a diterpenoid triepoxide isolated from Chinese herbal medicine *Tripterygium wilfordii* Hook F, possesses a myriad of pharmacological activities, including a powerful immunosuppressant effect on autoimmune disorders and potent anticancer activity [1,2]. In particular, many studies have demonstrated that TPL exhibits superior antiproliferative and antimetastatic effects against cancer cells, suppresses cancer-associated fibroblasts, and modulates immune microenvironment [3]. Being similar to some conventional small molecules like doxorubicin and paclitaxel, TPL also exhibits significant anticancer efficacy based on the previous studies. Various potential anticancer mechanisms of TPL have been revealed, including autophagy activation, cell cycle arrest, caspase-dependent cell death, anti-angiogenesis, and interference with epithelial–mesenchymal transition and metastasis [4,5]. Unfortunately, TPL exhibits remarkable biological activity, as well as server systemic toxicity and a narrow therapeutic window. Minnelide, an analog of TPL with better water solubility, has been clinically investigated for solid tumors, but a recent clinical trial has failed because of safety limitations [6]. Recently, combination therapy has become a routine strategy in cancer chemotherapy, with significant advantages over monotherapy, including lower therapeutic failure probability and slower development of drug resistance [7]. Likewise, the combination chemotherapeutic drugs with TPL could sensitize cancer cells to several chemotherapeutic drugs, such as doxorubicin, paclitaxel, cisplatin, and celastrol, with the synergistic anticancer efficacy [8–11]. However, considering intrinsic potential systemic toxicity of these cytotoxic agents, the combination therapy of chemotherapeutic agents would result in the superimposed side effects on the whole body [12-16]. Therefore, a novel combination therapy with high therapeutic outcome and low side-effect risk is still to be proposed.

Recently, PDT has attracted widespread attention for treatment of solid cancers because of its noninvasiveness and high tissue selectivity [17,18]. Based on the production of $^1O_2$ and ROS, resulting from the photosensitizer under laser irradiation, significant anticancer effects of PDT could be achieved [19,20]. However, the utilization of PDT still faces some challenges, such as insufficient tumor ablation capacity against deep tumors and the occurrence of peripheral tissue damage. Many attempts of using PDT combined with chemotherapy have been made to overcome the therapeutic drawbacks and adverse effects of monotherapy [21–27]. Therefore, TPL combined with Ce6, an acknowledged photosensitizer, could be a viable and effective strategy for cancer treatment. However, taking the different pharmacokinetic characteristics and cancer cellular internalization capacity of multiple agents into consideration, a variety of nanoscaled vehicles have been employed to co-load these combination agents, so as to enhance tumor accumulation, synchronous delivery, and even the specific release of the combination agents in response to kinds of stimuli. Yu et al. designed photoactivable liposomes incorporating Ce6 and TPL to facilitate their combination, showing the enhanced antitumor effect both *in vitro* and *in vivo* on a patient-derived tumor xenograft of HCC [28]. However, reversible lipid peroxides-dependent drug release, attributed to the reaction between allylic hydrogens in egg yolk lecithin and ROS generated by Ce6, would also be attenuated because of the weakness of laser penetration in this system. Thus, a novel stimuli-responsive nanocarrier with a more precise drug release profile is desired for the combination of PDT and chemotherapeutic benefit of TPL [29,30].

Among multiple endogenous distinctive characteristics of tumor microenvironment, acidic pH environment in tumor extracellular tissue (pH ~6.5) and endosomes/lysosomes of cancer cells (pH 4.0–6.0), compared with pH 7.4 in normal tissues, has been commonly utilized to develop pH-responsive nanosystems, to promote the specific drug release behavior in tumor sites [31-33]. In previous studies, numerous pH-sensitive nanocarriers have been developed based on the PBAEs co-polymer, which show strong “proton-sponge” effect and water solubility transformation in response to acidic pH value. We fabricated pH-responsive micelles composed by the self-assembly of PEG-PBAE co-polymer to achieve rapid drug release in tumor site [34–36]. However, relying on the critical CMC value, the stability of micelles during the blood circulation commonly confronts a big challenge, because they are prone to disassociation and premature release of the encapsulated payloads before reaching the tumor site. Although some strategies to lower the CMC value of amphiphilic block co-polymers have been suggested, this issue still urgently needs to be properly addressed [37,38].

Currently, supramolecular polymer micelles based on the host–guest interaction, with the high physical stability and strong inclusiveness, have received considerable interest; in these micelles, CDs have been extensively used to form inclusion complexes with linear polymers such as PEG [39-41]. Such encapsulation of co-polymer into CDs may increase the drug loading capacity and the stability of micellar structure [42]. As a proof of concept, we herein developed well-defined pH-responsive supramolecular micelles, based on the host–guest interactions between β-CD and PEG segment of mPEG-PBAE-mPEG co-polymer, to co-encapsulate TPL and Ce6 (TPL+Ce6/NPs). As shown in Fig. 1A, based on the self-assembly of mPEG-PBAE-mPEG, both TPL and Ce6 were co-loaded into flower-like micelles,

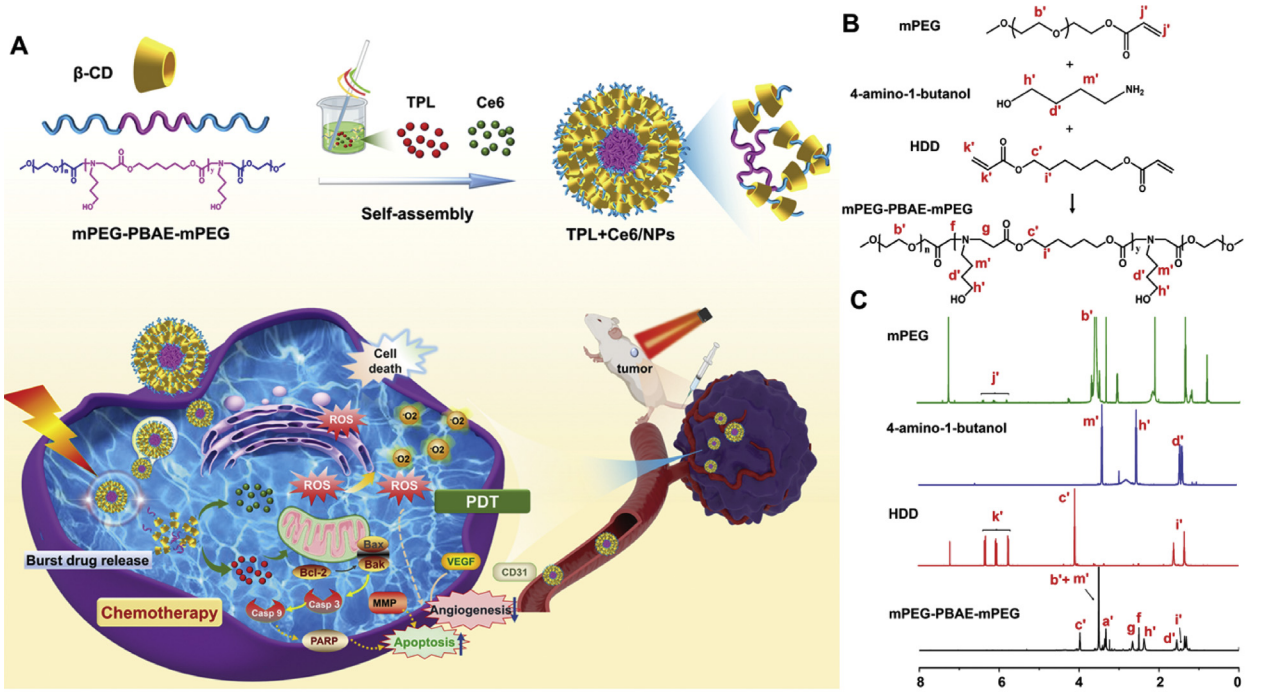

Fig. 1 – (A) Schematic representation of self-assembly of supramolecular TPL+Ce6/NPs and dual-synergistic combination therapy of chemotherapy and PDT. Synthetic route (B) and ^{1}H NMR spectrum (C) of mPEG-PBAE-mPEG.

in which PEG and PBAE act as the hydrophilic shell and the hydrophobic core, respectively. Nevertheless, mediated by the PEG's insertion into the hydrophobic internal cavity of β-CDs, a tight β-CD layer was embedded on the surface of mPEG-PBAE-mPEG micelles, which could effectively prevent the premature drug leakage. After the co-delivery of TPL and Ce6 into tumor tissue by EPR effects of NPs, the loaded payloads could be intelligently boosted in tumor acidic environments. In that way, the synergistic anticancer outcomes, resulting from TPL-initiated chemotherapy in combination with PDT by the laser activation of Ce6, could be achieved. To our knowledge, this is the first attempt to fabricate supramolecular pH-responsive micelles for the combination of PDT and chemotherapy, exhibiting high micellar stability and pH-triggered intracellular drug release and efficient suppression capacity for tumor growth and metastasis. Such a nanosystem may be an efficient strategy to overcome a series of obstacles in chemo-photodynamic therapy.

2. Materials and methods

2.1. *Materials*

Triptolide (TPL) was purchased from Chengdu DeSiTe Biological Technology Co., Ltd (Chengdu, China). Chlorin e6 (Ce6), HDD, TDP and β-CD was obtained from Shanghai Macklin Biochemical Co., Ltd (Shanghai, China). Hoechst 33,342 was purchased from Suzhou Yuheng Biotechnology Co., Ltd. (Suzhou, China). Cell culture medium and FBS were obtained from Invitrogen (Carlsbad, CA, USA). BCA protein quantitative detection kit and Annexin V-FITC/PI apoptosis kit was supplied by MultiScience (Lianke) Biotech Co., Ltd. (Hangzhou, China). Ki67, Bax, CD31, and VEFG were purchased from Wuhan Servicebio Technology Co., Ltd (Wuhan, China) Caspase 3, caspase 9, and PARP were obtained from Abcam (Abcam, Cambridge, UK). Other organic solvents or reagents were of analytic grade. HepG2 cells, B16 cells and H22 cells were purchased from Boster Biological Technology co.ltd (California, US). BALB/c nude mice (4 weeks old; 14–16 g) were purchased from SPF Biotechnology Co., Ltd. (Beijing, China).

2.2. *Synthesis and characterization of mPEG-PBAE-mPEG triblock co-polymer*

Five grams of 2 mmol methoxy PEG were placed into a two-neck flask, followed by heating under vacuum for 1.5 h at 90 °C. Subsequently, anhydrous toluene (25 ml), 6 mmol acryloyl chloride (0.49 ml), and 18 mmol TEA (2.5 ml) were added dropwise. The reaction was conducted at 45 °C for 15 h. After the insoluble triethylamine hydrochloride salt was removed by filtration, the acrylated mPEG was formed in ether solution via precipitation and then oven-dried.

The mPEG-PBAE-mPEG triblock co-polymer was prepared using the mPEG-A, HDD, and TDP via Michael-type step polymerization. The mPEG-A, HDD, and TDP were dissolved in chloroform. The reaction was performed for 24 h at 55 °C under N_2. The mPEG-PBAE-mPEG triblock co-polymer was obtained and purified after precipitation with diethyl ether, followed by vacuum drying. ^{1}H NMR was used to assess the structure of mPEG-PBAE-mPEG triblock co-polymer, and the molecular weight was determined by GPC [43].

2.3. Synthesis and characterization of TPL+Ce6/NPs

TPL+Ce6/NPs were prepared by a simple nanoprecipitation method via self-assembly processes in aqueous solution. In typical procedures, 30 mg of β-CD was first dissolved in water. Then, 4.2 mg of Ce6, 0.7 mg of TPL, and 15 mg of mPEG-PBAE-mPEG triblock co-polymer were co-dissolved in THF, and then mixed with water containing β-CD. After stirring for 2 h at ambient temperature, the mixture was evaporated for 10 min by a rotary evaporator to remove THF. After we removed the residual THF in NPs suspension, these unloaded drugs in suspension were removed by ultra-high speed centrifugation. The suspension was firstly centrifuged at 13 500 rpm for 40 min. And supernatant was discarded and the sediment was collected. Finally, TPL+Ce6/NPs were obtained by resuspending the sediment with water. The concentrations of TPL and Ce6 were measured by HPLC (mobile phases=water and methanol (53:46, v/v) and water and methanol (10:90, v/v); measurement wavelengths=220 and 450 nm, respectively).

2.4. pH-responsive ability of TPL + Ce6/NPs

After dispersing TPL+Ce6/NPs in PBS for more than 12 h at pH 5.8 with stirring at 100 rpm. The particle size was determined using a Zetasizer Nano ZS90 at the specified time points (0, 2, 4, 8, and 12 h).

2.5. Drug release from TPL+Ce6/NPs

Two milliliters of TPL+Ce6/NPs suspension were placed in a dialysis bag (cutoff MW, 5000) containing 50 ml of PBS (pH 5.8 or 7.4) and then dialyzed at 37 °C, 120 rpm in the oscillating incubator. One milliliter of samples was collected at each time interval, and an equal volume of dialysis medium was replenished. The drug release was used by the HPLC method, and the cumulative drug release was calculated.

2.6. Detections of pdt efficiencies of TPL+Ce6/NPs

Briefly, 25 μl of 50 μM SOSG was added into the solutions of free TPL, free Ce6, and TPL+Ce6/NPs, followed by 650-nm laser irradiation at 0.63 W/cm^2 for different time periods. The TPL and Ce6 concentrations were 40 and 180 μg/ml, respectively. Subsequently, oxidized SOSG was detected by a fluorescence spectrophotometer. The blank aqueous solution was used as a negative control.

2.7. Intracellular ROS measurement

HepG2 cells (2.0×10^5 cells/ml) were grown in a 24-well plate overnight. After incubated with different NPs formulations containing 54 nM of Ce6, the HepG2 cells were subjected to a 650 nm laser irradiation at 0.63 W/cm^2 for 6 min. Next, the cells were incubated for 4 h, and the media were discarded, followed by 20 μM DCFH-DA staining for 20 min. Quantitative analysis of intracellular DCF was conducted using the flow cytometer.

2.8. In vitro cytotoxicity efficacy

The cytotoxicity assays were assessed in HepG2 cells, B16 cells and H22 cells using the CCK-8 kit. HepG2 cells (6.0×10^4 cells/ml) were grown in a 96-well plate and exposed to the NPs for 48 h. Free TPL (5–160 nM), free Ce6 (13.5–432 nM), free Ce6+TPL and TPL+Ce6/NPs (with the molar ratio of TPL/ Ce6 at 1/2.7) at a series of concentrations were used to incubate with cells. Next, the cells were subjected to the 650-nm laser irradiation at 0.63 W/cm^2 for 5 min. B16 cells and H22 cells were treated in the same way. The CI value was used to evaluate the synergism of TPL and Ce6 co-treatment.

2.9. Mitochondrial membrane potential (MMP) and cell apoptosis assays

Free TPL, free Ce6, free Ce6+TPL and TPL+Ce6/NPs (20 nM TPL and 54 nM Ce6) were added into Hepg2 cells. The untreated cells were employed as negative controls. Next, the HepG2 cells were subjected to the 650 nm laser irradiation at 0.63 W/cm^2 for 5 min. After treatment for 48 h, the cells were incubated with JC-1 reagent for 20 min and stained with Annexin V-FITC and PI according to the manufacturer's instructions. Finally, the cells were measured by flow cytometry.

2.10. Cellular uptake in vitro

The uptake of TPL+Ce6/NPs by HepG2 cells was evaluated using the flow cytometry and confocal microscopy. Typically, HepG2 cells were grown in a 24-well plate overnight. Thereafter, the cells were exposed to TPL+Ce6/NPs, free TPL, or free Ce6 (54 nM Ce6) for 1 h, 2 h, 4 h and 8 h. CLSM was used to determine the intracellular localization and cellular internalization of TPL+Ce6/NPs. After staining with Hoechst (blue fluorescence) and phalloidin (green fluorescence) conjugates, the cells were visualized using CLSM.

2.11. Tumor accumulation imaging in vivo

Tumor-bearing mouse model was constructed by subcutaneously injecting H22 cells in 100 μl 50% Matrigel-containing PBS to the right axilla of nude mice (The certification of animal experiment ethics: permit CDU2019S121). The mice were assigned randomly to two groups and injection of free Ce6 and TPL+Ce6/NPs via the tail vein, respectively (an equal Ce6 amount of 4 mg/kg). IVIS Lumina Series imaging system was used to obtain images at a series of time points, including 1, 3, 6, 8, 12 and 24 post-injections. Finally, the tumors were collected from the sacrificed mice.

2.12. In vivo chemo-photodynamic therapy

Tumor xenograft model was established with H22 cells. The H22 xenograft tumor-bearing mice were divided into six groups (6 mice per group): untreated control (Saline), DOX, free TPL, free TPL+Ce6, TPL/NPs, and TPL+Ce6/NPs with irradiation. These groups were given every other day via

tail vein injection, with TPL dose of 0.3 mg/kg and Ce6 dose of 4 mg/kg. After 3 h and 12 h post-injection, the mice in the irradiation groups were subjected to the 650 nm laser irradiation at 0.63 W/cm^2 for 6 min. On completion of 14-d treatment, blood specimens were withdrawn from the sacrificed mice via eye puncture. The tumor and the main organs (including lung, heart, kidney, liver, and spleen) were isolated, and body weight and tumor measurements were obtained.

Moreover, B16 cells were used to establish another tumor xenograft model. B16 xenograft tumor-bearing mice were assigned randomly into seven groups (6 mice per group): control (Saline), DOX, free TPL, free Ce6 with irradiation, free TPL+Ce6, TPL/NPs, and TPL+Ce6/NPs with irradiation. The experimental method was consistent with that used for H22 xenograft tumor-bearing mice.

Subsequently, H&E, Ki67, Bax, CD31, and VEGF staining procedures were performed to further evaluate the tumor inhibition, apoptosis, and angiogenesis suppression efficacy. Furthermore, the levels of AST, ALT, BUN, and Cr were determined by blood biochemical analyzer. Moreover, the protein expression levels of caspase 3, caspase 9, and PARP in tumors were determined using western blot analysis (1:1000 dilution). The Pierce ECL assay (Thermo, Rockford, IL, USA) was used to examine the protein bands. The relative expression levels of the proteins were analyzed by ImageJ software.

2.13. Statistical analysis

All data were presented as mean ± standard deviation (SD) of three independent assays. Statistical difference between experimental results was assessed by one-way ANOVA. A P-value lower than 0.05 was considered statistically significant.

3. Results and discussion

3.1. Preparation and characterization of mPEG-PBAE-mPEG triblock co-polymer

PBAEs are common pH-responsive biodegradable polymers. Nanocarriers prepared by co-polymer of PEG and PBAE showed an obvious response to the changes of pH and were further used for drug delivery. The mPEG-PBAE-mPEG triblock co-polymer was synthesized by Michael-addition step polymerization of mPEG, HDD, and TDP, following a procedure similar to that reported in the literature [44]. The synthesis route is shown in Fig. 1B. The triblock co-polymer was verified by ^{1}H NMR spectrum (Fig. 1C), where the proton signals were recognized. The signal resonances at 2.46 ppm (f) and 2.79 ppm (g) were considered to correspond to protons of the newly formed methylene (-CH2) groups between the tertiary amine (NH3) and the esters (-COO). Intense peaks disappeared at 6 ppm (K'+J'), representing the complete conversion of the diacrylate monomers (CH_2=CHCOOR). Altogether, these results verified the successful synthesis of the polymer. The molecular weight of mPEG-PBAE-mPEG co-polymer was evaluated by GPC analysis (Fig. S1 in supplementary materials). The Mn of the co-polymer was 7.1 × 10^3 Da, and the dispersity index (Mw/Mn) was 1.12.

3.2. Synthesis and characterization of TPL+Ce6/NPs

TPL+Ce6/NPs showed a diameter of 156.0 nm (Fig. 2A), with a zeta potential of −13.2 mV. The loading capacity of TPL or Ce6 in TPL+Ce6/NPs were determined as 1.31%±0.01% and 6.77%±0.25%, and encapsulation efficiency of TPL or Ce6 were 98.27%±0.88% and 93.80%±1.44%, respectively. The combination molar ratio of TPL and Ce6 was 1/2.7. SEM and TEM images demonstrated a uniform size distribution and spherical morphology (Fig. 2D and 2E). We believe that the supramolecular structure contributed to the stability of the TPL+Ce6/NPs. Subsequently, the size changes and zeta potential of TPL+Ce6/NPs were evaluated to assess stability *in vitro* during 7 d storage. As shown in Fig. 2C, the size and zeta potential of TPL+Ce6/NPs remained relatively constant during the entire storage period, suggesting that TPL+Ce6/NPs had an excellent stability. Moreover, after one month of storage, the particle diameter remained between 156.0 nm and 165.0 nm, and the zeta potential remained between −12.0 mV and −15.0 mV.

FTIR was conducted to assess the intermolecular interaction between TPL, Ce6, and TPL+Ce6/NPs nanovehicle. As shown in Fig. 2I, the FTIR spectrum of TPL displayed characteristic peaks at 1721 cm^{-1} and 3455 cm^{-1}, which corresponded to the carbonyl and hydroxyl groups in lactonic ring, respectively. Meanwhile, the FT-IR spectrum of Ce6 displayed characteristic peaks at 1711 cm^{-1} and 3293 cm^{-1}, which represented the stretching vibrations of C–O and O–H, respectively. These peaks disappeared in the FTIR spectrum of TPL+Ce6/NPs, suggesting that TPL and Ce6 were not physically mixed but completely encapsulated in the NPs.

In the FTIR spectrum of mPEG segment (Fig. S2 in supplementary materials), characteristic peaks were observed at 1108 cm^{-1} (C–O-C bending vibration), 1466 cm^{-1} (C–O-C bending vibration), and 2888 cm^{-1} (C–H stretching), indicating the presence of these components. In the FTIR spectrum of β-CD, the apparent characteristic peaks at 1644 cm^{-1} and 3382 cm^{-1} were ascribed to the O–H bending and O–H stretching vibrations, respectively. In comparison with the spectrum of mPEG, the intensities of the peaks at 1466 cm^{-1} and 2888 cm^{-1} for TPL+Ce6/NPs were much lower because the carbonyl groups of the mPEG chains were included in β-CD cavities.

3.3. In vitro release of TPL from TPL+Ce6/NPs

In response to acidic conditions (pH 5.8) that mimic the acidosis of the tumor microenvironment, multiple peaks were detected (Fig. S3 in supplementary materials). In addition, TEM revealed the morphological changes in TPL+Ce6/NPs after 12 h incubation in the acidic solution (pH 5.8). As displayed in Fig. S4, TPL+Ce6/NPs almost completely disintegrated, and even fragment dispersion occurred. These results indicate that TPL+Ce6/NPs enhance the degradation of PBAE due to protonation of tertiary amine group residues, thereby leading to better drug release in the tumor microenvironment.

The above results suggest that TPL could be released from TPL+Ce6/NPs in a controlled way. Therefore, we further evaluated the *in vitro* release of TPL in PBS (pH 7.4) supplemented with acidic solution (pH 5.8) from TPL+Ce6/NPs

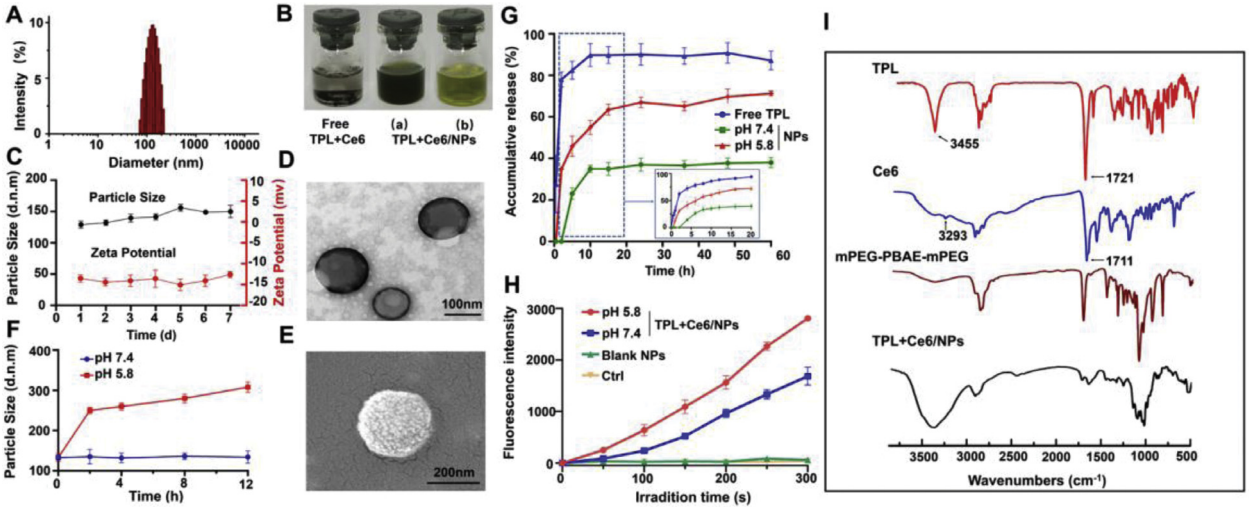

Fig. 2 – Characterization of TPL+Ce6/NPs. Characterization of TPL+Ce6/NPs. (A) Particle size distribution by DLS determination. (B) Representative photos of indissoluble suspension of free TPL and Ce6 physical mixture, and aqueous suspension of TPL+Ce6/NPs. (a represents a high concentration and b represents a low concentration). (C) Storage stability at 4 °C for 7 d (D) TEM and (E) SEM images of TPL+Ce6/NPs. pH-responsive particle size changes (F), drug release profiles (G) and singlet oxygen production efficiency by SOSG probe determination (H) of TPL+Ce6/NPs in response to different pH values. (I) FTIR spectra of TPL+Ce6/NPs, mPEG-PBAE-mPEG polymer and the payload agents.

using the dialysis method. As shown in Fig. 2G, TPL in NPs was released much slower than free TPL in the initial 20 h. In particular, the release of the TPL from NPs at pH7.4 is extremely slow, with only 38% within 20 h. In contrast, free TPL was released rapidly, reaching about 89% of TPL release during 10 h. However, the TPL release was significantly accelerated in the acidic solution, especially during the first 10 h, eventually leading to the release of 70% of TPL from TPL+Ce6/NPs by 20 h. Considering the lower pH levels in cancer cells (lower than 6.5), we deduced that TPL+Ce6/NPs could achieve the controlled release of TPL in tumor cells.

3.4. *Production of singlet oxygen*

The generation of $^1O_2$ by the photosensitizer irradiated at a suitable wavelength is one of the crucial mechanisms of PDT for inhibiting tumor growth [45]. We assessed the PDT efficiencies of TPL+Ce6/NPs after laser irradiation for different time periods using SOSG, a highly selective indicator for $^1O_2$, which was used as a fluorescence probe [46]. As shown in Fig. 2H, no fluorescence was observed either in PBS as control group or in blank NPs and free TPL. However, there was obvious increase in fluorescence for TPL+Ce6/NPs or free Ce6 upon irradiation, indicating their comparable $^1O_2$ production capability. ROS generation induced by TPL+Ce6/NPs was much stronger than that induced by free Ce6, implying that TPL+Ce6/NPs could enhance the photostability of Ce6.

3.5. *Cytotoxicity of TPL+Ce6/NPs against HepG2 cells and B16 cells*

As shown in Fig S5 and Table S1, the IC_{50} values of TPL in HepG2 and B16 cells were 14.86 and 79.32 nM, respectively. The IC_{50} values of Ce6 in HepG2 and B16 cells were 76.28 and 155.50 nM, respectively. It indicated that TPL exhibits the stronger cell proliferation suppress effect than Ce6. Therefore, when we optimized the preparation technology of TPL+Ce6/NPs, we set the molar ratio of TPL /Ce6 as 1/3, by means of regulating the feeding drug amounts. In fact, the encapsulated ratio of TPL and Ce6 in NPs was about 1/2.7. Furthermore, As shown in Table S1 in supplementary materials, when the combination ratio of TPL and Ce6 at 1/2.7, the CI values of TPL+Ce6 on HepG2 and B16 cells were 0.94 and 0.57, respectively. The CI values were lower than 1, it indicated that the combination ratio of TPL and Ce6 at 1/2.7 had a synergistic cytotoxic effect. According to these results, the combination of TPL and Ce6 with molar ratio 1/2.7 was selected for subsequent experiments.

In order to investigate the synergistic therapeutic effects of TPL+Ce6/NPs *in vitro* cytotoxicity of HepG2 cells, B16 cells and H22 cells was determined with CCK-8 assay. As shown in Fig. 3B and 3D, free Ce6 was almost nontoxic without irradiation in HepG2 cells and B16 cells, and no significant cytotoxicity was found in blank NPs with/without irradiation after incubation for 48 h. Next, we measured the inhibitory effects of free TPL, free Ce6, free TPL+Ce6, and TPL+Ce6/NPs in different media (pH 5.8 and 7.4) against HepG2 cells and B16 cells with 650 nm light irradiation (630 mW/cm^2, 3 min) under equal amounts of TPL and Ce6 (20 nM TPL equivalent and 54 nM Ce6 equivalent). As shown in Fig. 3A and 3C, at pH of 7.4, TPL+Ce6/NPs had lower cell proliferation ability compared with free TPL, free Ce6, and free TPL+Ce6, indicating that TPL+Ce6/NPs had much higher cytotoxicity. The superior cytotoxicity of TPL+Ce6/NPs resulted from these following advantages, including the higher cellular uptake mediated by nanovehicles, the synergetic anticancer effect of TPL and photodynamic therapeutic activity of Ce6 and the acid pH

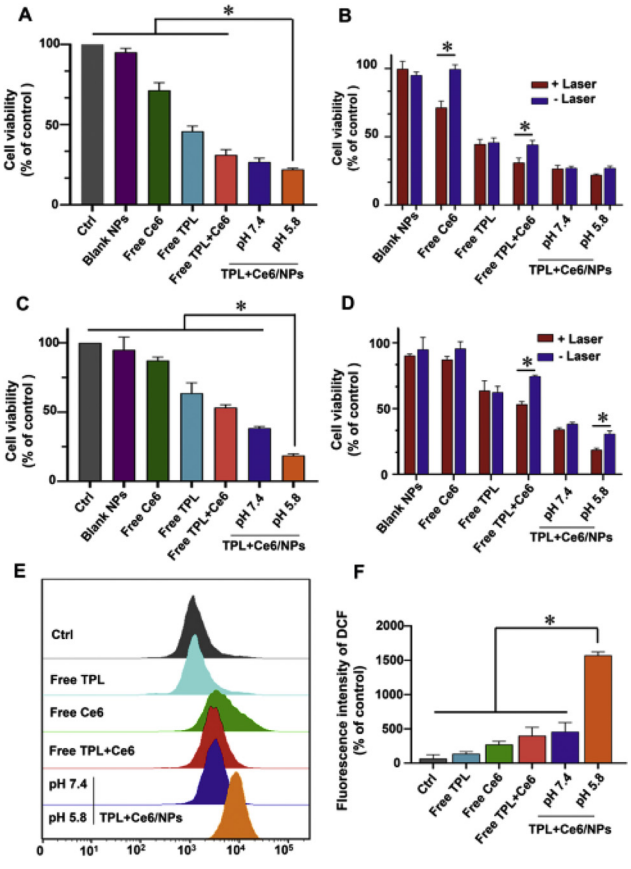

Fig. 3 – Synergistic cytotoxicity of TPL+Ce6/NPs in HepG2 and B16 cells for 48 h treatment. Cytotoxicity of TPL+Ce6/NPs, containing 20 nM TPL and 54 nM Ce6 equivalently, against HepG2 cells (A) and B16 cells (C) with laser irradiation after 48-h treatments. Comparison of cytotoxicity between different groups with laser or without laser irradiation in HepG2 cells (B) and B16 cells (D). Relative ROS generation of cells after various treatments by FCM analysis (E). The produced ROS amounts in different groups (F). *P < 0.05 indicates a statistically significant difference between groups.

responsive drug boost in endo/lysosome ascribed to PBAE polymer blocks. Particularly, when TPL+Ce6/NPs were used to treat cells in the culture medium with the different pH values, TPL+Ce6/NPs (pH 5.8) displayed the superior cell proliferation suppression effects on both HepG2 and B16 cells, in comparison to that at pH 7.4, due to the potential endo/lysosomes escape derived from proton sponge effect of PBAE polymers.

Furthermore, the higher cytotoxicity of TPL+Ce6/NPs against B16 cells at pH 5.8 than that at pH 7.4 could be observed in Fig. 3C. Although there is non-significant difference against HepG2 cells between at pH 5.8 and at pH 7.4, TPL+Ce6/NPs (pH 5.8) also exhibited the slightly lower cell viability, compared to that at pH 7.4 (Fig. 3A). TPL+Ce6/NPs at pH 7.4 exhibited the strong proliferation suppression effect, in which about 25% of cell viability could be determined. Therefore, TPL+Ce6/NPs at pH 5.8 were difficult to exhibit the higher cytotoxicity than that at pH 7.4 with significant difference. Moreover, the cytotoxicity profile of H22 cells was similar to that of HepG2 cells and B16 cells. TPL+Ce6/NPs at pH 5.8 exhibited much lower cell viability than other counterparts (Fig. S6 in supplementary materials). Therefore, these results indicate that the combined treatment with PDT and chemotherapy of TPL+Ce6/NPs results in enhanced tumor cell cytotoxicity, which is deem that the design of pH-responsive capacity in TPL+Ce6/NPs could facilitate the anticancer effects.

3.6. *Regulation of laser-triggered oxidation*

We evaluated the ROS production of TPL+Ce6/NPs via DCFH-DA assays. ROS have been considered key factors in killing tumor cells as they create irreversible injury [47]. As shown in Fig. 3E and 3F, triggered by laser irradiation, TPL+Ce6/NPs in pH 5.8 media showed a remarkably higher fluorescence intensity than free Ce6 and TPL+Ce6/NPs in pH 7.4 media. The high fluorescence intensity of TPL+Ce6/NPs may be attributed to effective internalization of NPs, thereby showing great ROS performance under the PDT effect.

3.7. *TPL+Ce6/NPs enhance cell apoptosis*

The decline in MMP is one of the early events of cell apoptosis, and we used JC-1 as an FCM biomarker to assess the changes in MMP values [48,49]. As shown in Fig. 4A and 4B, after treatment with free TPL, free Ce6, free TPL+Ce6, and TPL+Ce6/NPs at pH 7.4, the ratios of JC-1 green/red fluorescence changed slightly. However, the TPL+Ce6/NPs at pH 5.8 led to a remarkable decrease in the ratios of JC-1 green/red fluorescence. These results clearly show that the anticancer efficiency of the combination therapy is obviously enhanced in response to the acidic environment of the tumor.

TPL is involved in apoptosis of cancer cells. Thus, we further examined the antitumor effect of TPL+Ce6/NPs on HepG2 cell apoptosis as well as the underlying mechanisms. Annexin V-FITC/PI apoptosis assays were conducted to compare TPL alone, Ce6 alone, free TPL +Ce6, TPL+Ce6/NPs, and control groups with different media of pH 5.8 and 7.4 by flow cytometry. As shown in Fig. 4C and 4D, HepG2 cells were incubated with equal amounts of 20 nM TPL and 54 nM Ce6 for 48 h, and the apoptotic rates of TPL+Ce6/NPs were markedly higher than those of free TPL, free Ce6, and free TPL+Ce6. In particular, the highest apoptotic rate was observed for TPL+Ce6/NPs at pH 5.8. Surprisingly, compared with TPL-based chemotherapy group, the TPL+Ce6/NPs synergistic therapy group increased late-stage apoptosis twofold.

3.8. *Cellular uptake of TPL+Ce6/NPs*

The intracellular distribution of TPL+Ce6/NPs in HepG2 cells was assessed by CLSM. As displayed in Fig. 5A and S7-S9, Ce6 showed red fluorescence, and the fluorescence intensity of TPL+Ce6/NPs was significantly higher than that of free Ce6 and free TPL+Ce6, indicating that the intracellular internalization ability of TPL+Ce6/NPs was enhanced. Moreover, the cellular uptake of TPL+Ce6/NPs

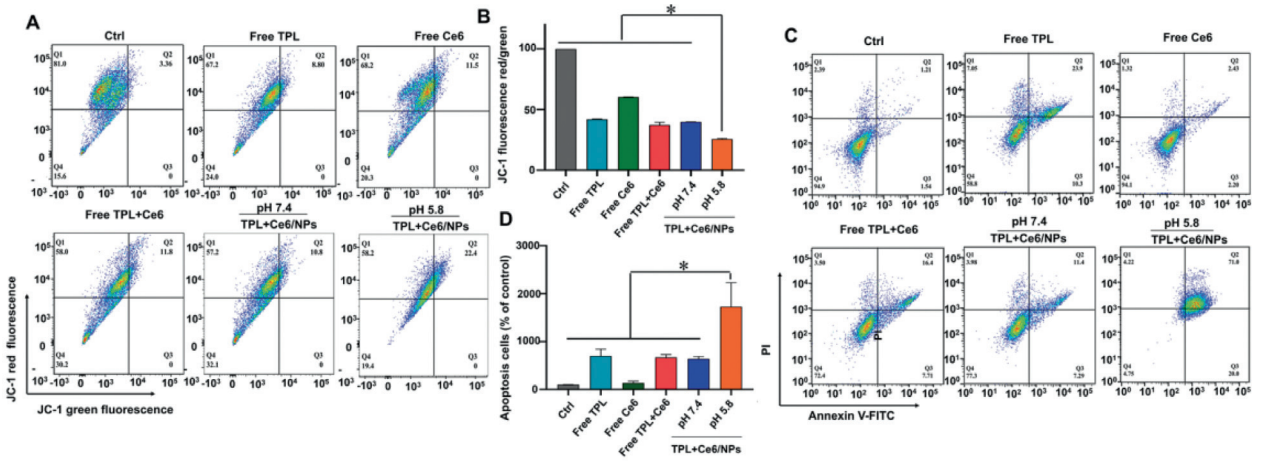

Fig. 4 – Mitochondrial membrane potential and cell apoptosis rate determination of HepG2 cells induced by TPL+Ce6/NPs. Mitochondrial membrane potential determination of HepG2 cells treated with TPL+Ce6/NPs (including equivalently 20 nM TPL and 54 nM Ce6) for 48 h, using JC-1 dye staining by FCM analysis (A, B). Cell apoptosis of HepG2 cells treated with TPL+Ce6/NPs (including equivalently 20 nM TPL and 54 nM Ce6) for 48 h, using Annexin V-FITC and PI double staining by FCM analysis. (C, D). *P < 0.05 indicates a statistically significant difference between groups.

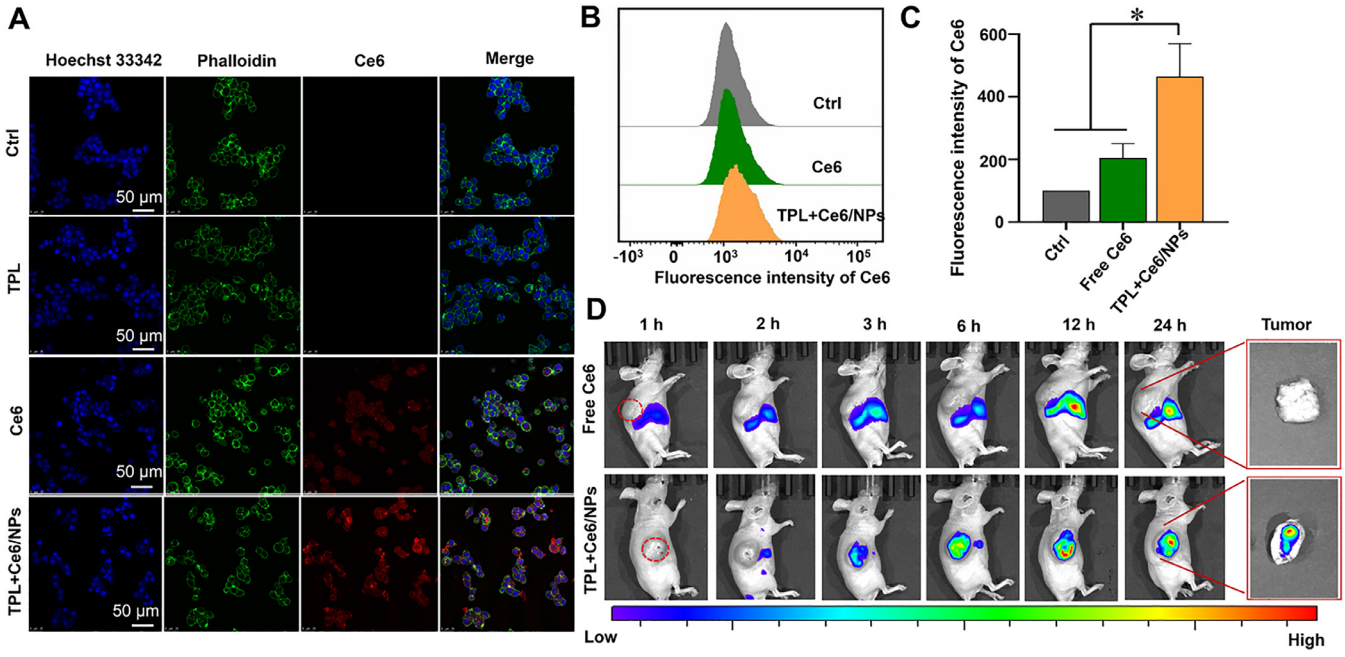

Fig. 5 – Cellular uptake in HepG2 and *in vivo* tumor accumulation of Ce6/NPs. (A) Representative cellular uptake images of HepG2 cells after incubation with TPL+Ce6/NPs for 4 h by CLSM observation. Hoechst 33,342 and phalloidin were employed to stain cell nucleus and cytoskeleton. The scale bar is 50 μm. (B, C) Quantitative intracellular fluorescence determination in HepG2 cells with treatment of free Ce6, free TPL and TPL+Ce6/NPs, respectively for 4 h by FCM. *P < 0.05 indicates TPL+Ce6/NPs *versus* free Ce6 group. (D) *In vivo* real-time imaging study of H22 tumor-bearing mice after intravenous injection of Ce6/NPs or free Ce6 at different time intervals. At 24 h post-injection, tumors were harvested and observed by *ex vivo* fluorescent imaging.

during 8 h incubation was much higher than free Ce6 at each time point. And the cellular uptake of TPL+Ce6/NPs exhibited the time-dependent manner. The increased cellular uptake is due to TPL+Ce6/NPs entering the cells through endocytosis instead of passive diffusion. In addition, the quantitative data of flow cytometric analysis (Fig. 5B and 5C) agreed well with the qualitative data. This suggests that TPL+Ce6/NPs can act as a suitable carrier to intellective deliver drugs into tumor cells, and exert the dual effects of chemotherapy and photodynamic therapy.

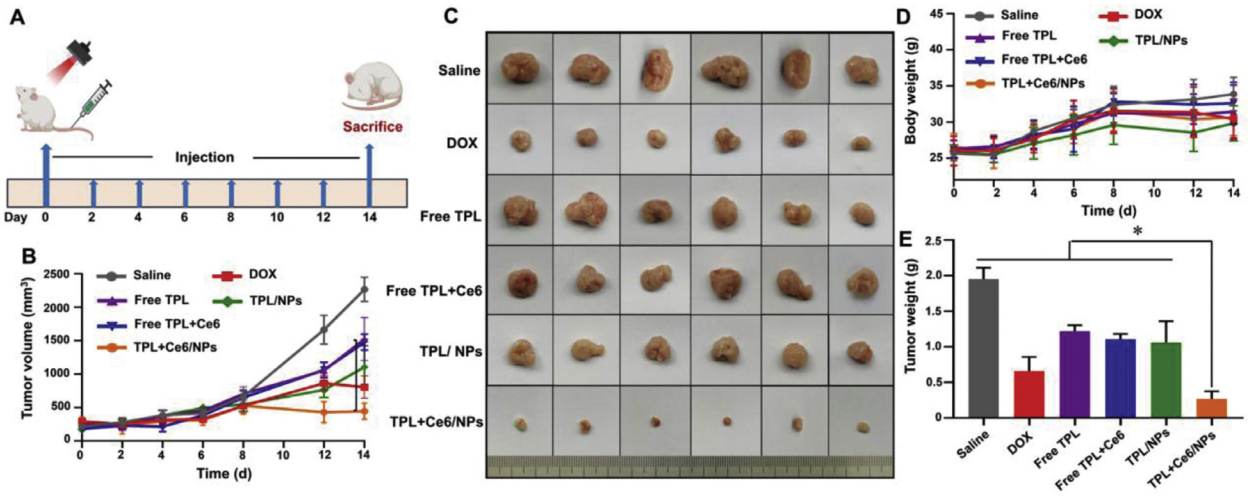

Fig. 6 – *In vivo* anti-tumor effects of TPL+Ce6/NPs in H22-bearing tumor mice model. (A) Schematic illustration for the experimental regimen in H22 tumor-bearing mice. (B) Tumor growth curves of different groups in the whole experiment period. (C) Representative photographs of tumors excised from each treatment group on day 14. *Ex vivo* photographs of tumors are vertically aligned top-to-bottom according to the left-to-right whole-animal images. (D) Body weight changes of H22 tumor-bearing mice in the whole experiment period. (E) Weight of these harvested tumor tissues. *P < 0.05 indicates a statistically significant difference between groups.

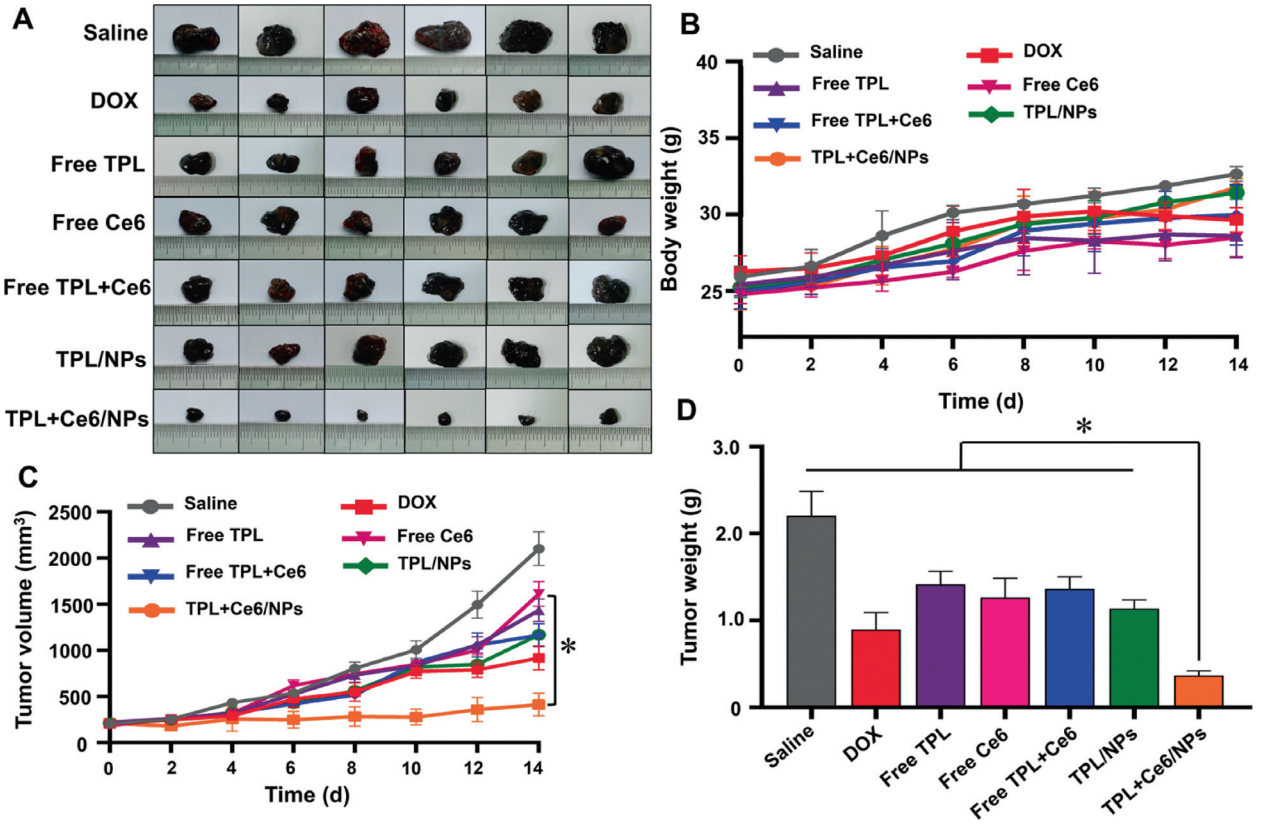

Fig. 7 – *In vivo* anti-tumor effects of TPL+Ce6/NPs in B16-bearing tumor mice model. (A) Representative photographs of tumors excised from each treatment group on day 14. (B) Body weight changes of B16 tumor-bearing mice in the whole experiment period. (C) Tumor growth curves of different groups in the whole experiment period. (D) Body weight changes of B16 tumor-bearing mice in the whole experiment period. *P < 0.05 indicates a statistically significant difference between groups.

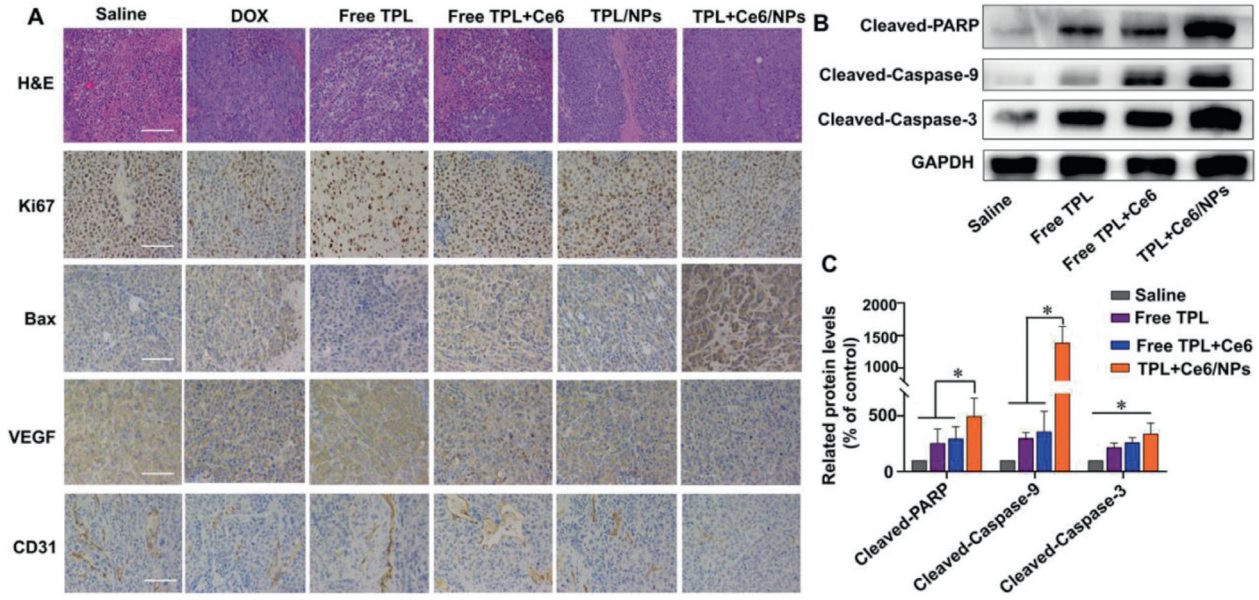

Fig. 8 – Immunohistochemical staining and western blot analysis of tumor tissues derived from H22-bearing tumor mice. (A) H&E staining and immunohistochemistry staining of Ki-67, Bax, VEGF, and CD31. The scale bar is 50 μm. (B) The expression of mitochondrial apoptosis pathway-relative proteins (PARP, caspase 3, and caspase 9) evaluated by western blot. (C) Semiquantitative evaluation of the expression level of these proteins. *$P < 0.05$ indicates a statistically significant difference between groups.

3.9. *In vivo distribution of TPL+Ce6/NPs*

The performance of TPL+Ce6/NPs was further assessed in H22 tumor-bearing nude mice. The mice received free Ce6 and TPL+Ce6/NPs. As shown in Fig. 5D, a gradual accumulation of TPL+Ce6/NPs at tumor sites was observed within the first 3 h after treatment. Higher fluorescence intensity of TPL+Ce6/NPs was observed compared with that of free Ce6. At 24 h after the injection, a significant fluorescence signal was still detected at the tumor site. Furthermore, TPL+Ce6/NPs-treated mice displayed stronger fluorescence intensity than those treated with free Ce6, especially at the tumor tissue. Such evidence suggests that long circulation in mice and accumulation of TPL and Ce6 in tumor sites can be efficiently improved by TPL+Ce6/NPs to full play to PDT and chemotherapy.

3.10. *In vivo chemo-photodynamic therapy with TPL+Ce6/NPs*

To verify that TPL+Ce6/NPs have a preferable antitumor effect, we adopted H22 and B16 subcutaneous tumor-bearing mouse models to achieve synergistic effects of TPL+Ce6/NPs for effectively inhibiting tumor growth. As illustrated in Fig. 6A, from Day 0 to 14, the mice were exposed to saline, DOX, free TPL, free Ce6+TPL, TPL/NPs, or TPL+Ce6/NPs for seven times. In H22 model, the tumor growth and body weight curves were recorded every 2 d after treatment for a total of 14 d. As shown in Fig. 6B, all experimental groups exhibited a lower tumor growth rate than the saline group. Very weak antitumor efficacy was achieved using free TPL and free TPL+Ce6. In the meantime, only moderate tumor inhibition was found in the groups administered with DOX and TPL/NPs, but tumor reduction was achieved compared with the saline group. The strongest antitumor effect was observed for the group treated with TPL+Ce6/NPs by laser irradiation. When the drug enters the tumor cells, it is rapidly released from the nanoparticles via the stimulation by low pH, thereby improving the effect of inhibiting tumor growth. The size of the tumor after different treatments is shown in Fig. 6C. Furthermore, the tumor weight (Fig. 6E) showed a similar trend to the tumor volume in each group. These findings indicate the synergistic efficacy of PDT and chemotherapy.

Meanwhile, the B16 tumor model was established to further determine the antitumor efficacy by PDT and chemotherapy *in vivo*. At present, the clinical application of PDT involves intravenous injection of a photosensitizer. Therefore, in the B16 tumor model, we used the free Ce6 group to explore whether nanoparticles can increase the antitumor effect compared with the free photosensitizer. The treatment period was consistent with that of the H22 tumor model. As shown in Fig. 7A, remarkable difference was observed between the groups. Compared with the saline group, the free Ce6 group, the free TPL, and the free TPL+Ce6 group exhibited minimal antitumor effect. In contrast, the TPL+Ce6/NPs group showed a remarkable antitumor effect and obviously reduced the tumor volume (Fig. 7C). As shown in Fig. 7D, the tumor weight of TPL+Ce6/NPs-treated group was the lowest among all groups, and this result was consistent with the tumor volume. The body weight in each of the treatment groups remained constant throughout the treatment period (Fig. 7B).

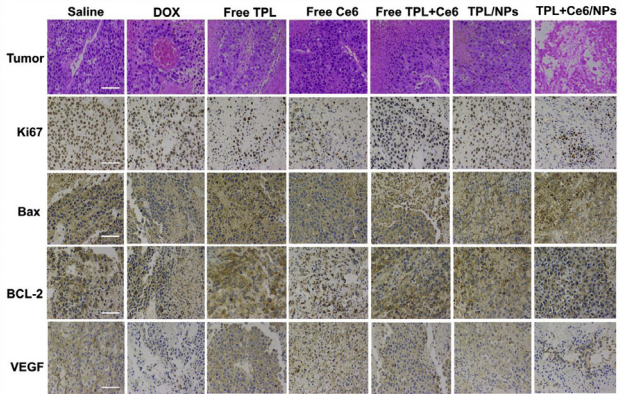

Fig. 9 – Immunohistochemical staining of tumor tissues derived from B16-bearing tumor mice. H&E staining and immunohistochemistry staining of Ki-67, Bax, BCL-2, and VEGF. The scale bar is 50 μm.

3.11. *Potential antitumor mechanisms*

To further confirm the antitumor effects at histological level, we excised tumors and organs in the H22 tumor model and the B16 tumor model, and prepared H&E and immunohistochemical stainings. As shown in Fig. 8A, in the H22 tumor model, severe apoptotic damage and even necrocytosis were found in the tumors of the TPL+Ce6/NPs-treated group compared with both free TPL and free Ce6+TPL treated groups, which was consistent with the abovementioned animal experiment results. These findings were also evaluated by immunohistochemistry for Ki67 and Bax; the number of Ki67-positive cells in TPL+Ce6/NPs-treated group was much lower than that in the other groups, while the number of Bax-positive cells was higher than that in the other groups. In our previous studies, we have confirmed the ability of TPL to suppress angiogenesis and thus inhibit tumor growth [36,50]. Herein, the expression levels of CD31 and VEGF were significantly reduced in the TPL+Ce6/NPs group compared with the remaining groups, indicating the excellent antiangiogenic ability of TPL+Ce6/NPs. The H&E images of tumors and the levels of Ki67, Bax, and VEGF in the B16 tumor model were consistent with those in the H22 tumor model (Fig. 9). Moreover, compared with the other groups, the expression of Bcl-2 in the B16 tumor model was significantly declined in the TPL+Ce6/NPs group.

Furthermore, to validate the regulatory effect of TPL+Ce6/NPs combining PDT and chemotherapy on tumor growth, WB analysis was also employed on the H22 model tumor tissue to evaluate the levels of apoptosis pathway proteins such as PARP, caspase 3, and caspase 9. As displayed in Fig. 8B and 8C, TPL+Ce6/NPs remarkably elevated the protein levels of PARP, caspase 3, and caspase 9 compared with control, free TPL, or free TPL+Ce6 groups. These results indicated that TPL+Ce6/NPs markedly induced tumor cell apoptosis and thereby inhibited tumor growth.

Considering the severe toxicity of TPL, we should assess the toxic effect of TPL+Ce6/NPs, despite excellent antitumor effects. Therefore, we performed H&E staining on the major organs and analyzed blood biochemical indexes in both H22 and B16 models. As shown in Fig. 10A and S10, the liver histopathological lesions in the free TPL group were more severe than those in the saline group, manifesting as fat vacuoles, infiltration by inflammatory cells, and necrosis; however, the TPL+Ce6/NPs group had less severe lesions, suggesting that liver injury is caused by administration of free TPL. In addition, ALT and AST levels in blood were significantly higher in the free TPL group than in the saline

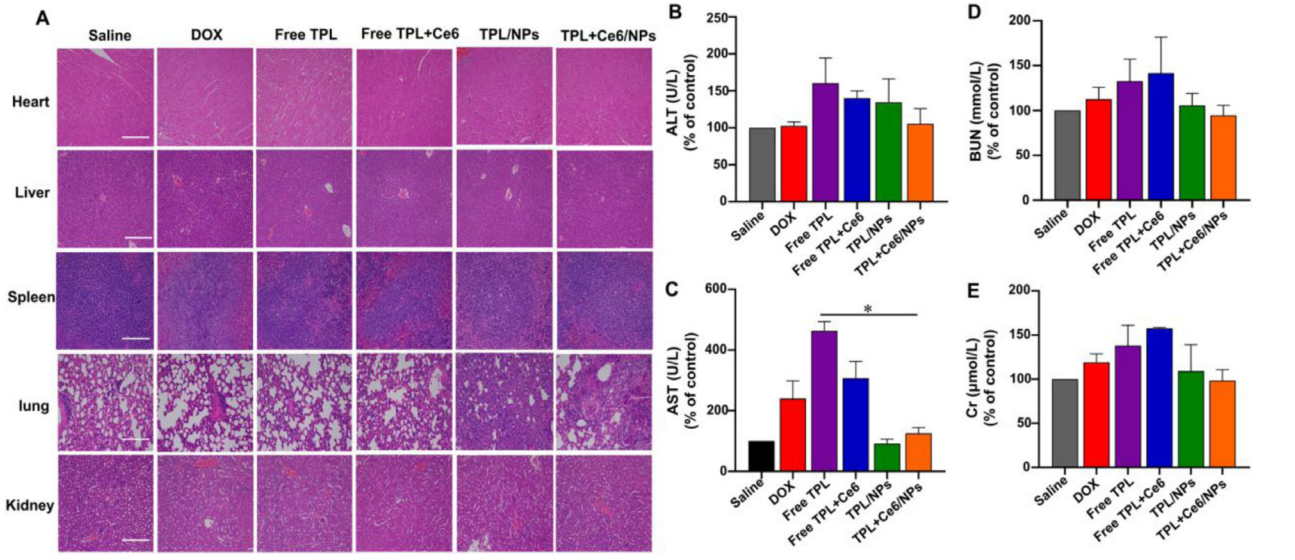

Fig. 10 – Histological analyses of main organs and blood biochemical indexes derived from H22-bearing tumor mice. (A) H&E histological analyses of main organs after various treatments of the H22 tumor model. The content of ALT(B), AST(C), BUN(D), and Cr(E) in blood after treatment. The scale bar is 50 μm. *$P < 0.05$ indicates a statistically significant difference between groups.

group (Fig. 10B, 10C, S11A and S11B). In contrast, there were no significant changes in those biochemical indexes after the administration of TPL+Ce6/NPs. No remarkable differences in the concentrations of BUN and Cr were found among the groups. The results were identical in the B16 model (Fig. 10D, 10E, S11C and S11D)

4. Conclusion

In summary, we successfully developed pH-sensitive supramolecular TPL+Ce6/NPs. The supramolecular structure ensured efficient drug encapsulation and excellent stability, which is more appropriate for future applications in synergistic antitumor treatment. The obtained TPL+Ce6/NPs displayed significant pH-responsiveness and performed the controlled release of TPL in a mimicked-pH condition to exert cytotoxicity. Simultaneously, the release of Ce6 produced more singlet oxygen species to improve the antitumor effect. Hence, laser-irradiated TPL+Ce6/NPs remarkably inhibited tumor cell proliferation in HepG2 cells and B16 cells. The combined application of PDT and chemotherapy achieved a great inhibitory effect on tumor growth in H22 and B16 tumor xenograft models with minimal side effects. Histological, immunofluorescence, and immunohistochemical analyses further illustrated that TPL+Ce6/NPs achieved synergistic anticancer effects by inducing apoptosis. In conclusion, supramolecular systems have the potential to provide dual treatments for the synergistic combination of PDT and chemotherapy for cancer treatment.

Conflicts of interest

The authors declare no competing financial interest.

Acknowledgement

This work was supported by National Natural Science Foundation of China (No.81973662), Distinguished Young Scholar of Sichuan Provincial Science and Technology Department (No.2019JDJQ0049), and 111 Project (No.B18035). We express our gratitude to Jiayi Sun at Innovative Institute of Chinese Medicine and Pharmacy, Chengdu university of Traditional Chinese Medicine, for help with CLSM.

Supplementary materials

Supplementary material associated with this article can be found, in the online version, at doi:10.1016/j.ajps.2021.12.003.

REFERENCES

[1] Noel P, Hoff DDV, Saluja AK, Velagapudi M, Borazanci E, Han HY. Triptolide and its derivatives as cancer therapies. Trends Pharmacol Sci 2019;40(5):327–41.

[2] Chen SR, Dai Y, Zhao J, Lin LG, Wang YT, Wang Y. A mechanistic overview of triptolide and celastrol, natural products from *tripterygium wilfordii* Hook F. Front Pharmacol 2018;9:104.

[3] Gao J, Zhang YF, Liu XH, Wu XY, Huang LQ, Gao W. Triptolide: pharmacological spectrum, biosynthesis, chemical synthesis and derivatives. Theranostics 2021;11(15):7199–221.

[4] Hou W, Liu B, Xu HT. Triptolide: medicinal chemistry, chemical biology and clinical progress. Eur J Med Chem 2019;176:378–92.

[5] Hou ZY, Tong XP, Peng YB, Zhang BK, Yan M. Broad targeting of triptolide to resistance and sensitization for cancer therapy. Biomed Pharmacother 2018;104:771–80.

[6] Xu HT, Liu B. Triptolide-targeted delivery methods. Eur J Med Chem 2019;164:342–51.

[7] Lee D, Jang SY, Kwon S, Lee Y, Park E, Koo H. Optimized combination of photodynamic therapy and chemotherapy using gelatin nanoparticles containing tirapazamine and pheophorbide a. ACS Appl Mater Interfaces 2021;13(9):10812–21.

[8] Wu B, Lu ST, Zhang LJ, Zhuo RX, Xu HB, Huang SW. Codelivery of doxorubicin and triptolide with reduction-sensitive lipid-polymer hybrid nanoparticles for *in vitro* and *in vivo* synergistic cancer treatment. Int J Nanomedicine 2017;12:1853–62.

[9] Liu J, Cheng H, Han L, Qiang Z, Zhang XW, Gao W, et al. Synergistic combination therapy of lung cancer using paclitaxel-and triptolide-coloaded lipid-polymer hybrid nanopartices. Drug Des Devel Ther 2018;12:3199–209.

[10] Ho JN, Byun SS, Lee S, Oh JJ, Hong SK, Lee SE, et al. Synergistic antitumor effect of triptolide and cisplatin in cisplatin resistant human bladder cancer cells. J Urol 2015;193(3):1016–22.

[11] Ramamoorthy P, Dandawate P, Jensen RA, Anant S. Celastrol and triptolide suppress stemness in triple negative breast cancer: notch as a therapeutic target for stem cells. Biomedicines 2021;9(5):482.

[12] Xie JH, Lu Y, Yu BQ, Wu J, Liu J. Galactose-modified enzymatic synthesis of poly(amino-co-ester) micelles for co-delivery miR122 and sorafenib to inhibit hepatocellular carcinoma development. Chinese Chemical Letters 2020;31(5):1173–7.

[13] Yang L, Xu J, Xie Z, Song F, Wang X, Tang R. Carrier-free prodrug nanoparticles based on dasatinib and cisplatin for efficient antitumor *in vivo*. Asian J Pharm Sci 2021;16(6):762–71.

[14] Lin CC, Tong F, Liu R, Xie R, Lei T, Chen YX, et al. GSH-responsive SN38 dimer-loaded shape-transformable nanoparticles with iRGD for enhancing chemo-photodynamic therap. Acta Pharm Sin B 2020;10(12):2348–61.

[15] Liu R, An Y, Jia WF, Wang YS, Wu Y, Zhen YH, et al. Macrophage-mimic shape changeable nanomedicine retained in tumor for multimodal therapy of breast cancer. J Control Release 2020;321:589–601.

[16] Yu WQ, He XQ, Yang ZH, Yang XT, Xiao W, Liu R, et al. Sequentially responsive biomimetic nanoparticles with optimal size in combination with checkpoint blockade for cascade synergetic treatment of breast cancer and lung metastasis. Biomaterials 2019;217:119309.

[17] Wang WL, Lin L, Ma XJ, Wang B, Liu SR, Yan XX, et al. Light-induced hypoxia-Triggered living nanocarriers for synergistic cancer therapy. ACS Appl Mater Interfaces 2018;10(23):19398–407.

[18] Shen LJ, Zhou TJ, Fan YT, Chang X, Wang Y, Sun JG, et al. Recent progress in tumor photodynamic immunotherapy. Chinese Chemical Letters 2020;31(7):1709–16.

[19] Kessel D. Photodynamic therapy: apoptosis, paraptosis and beyond. Apoptosis 2020;25(9–10):611–15.
[20] Lee J, Jenjob R, Davaa E, Yang SG. NIR-responsive ROS generating core and ROS-triggered 5′-Deoxy-5-fluorocytidine releasing shell structured water-swelling microgel for locoregional combination cancer therapy. J Control Release 2019;305:120–9.
[21] Zhao J, Duan L, Wang AH, Fei JB, Li JB. Insight into the efficiency of oxygen introduced photodynamic therapy (PDT) and deep PDT against cancers with various assembled nanocarriers. Wiley Interdiscip Rev Nanomed Nanobiotechnol 2020;12(1):e1583.
[22] Shen LJ, Zhou TJ, Fan YT, Chang X, Wang Y, Sun JG, et al. Recent progress in tumor photodynamic immunotherapy. Chinese Chemical Letters 2020;31(7):1709–16.
[23] Chen HZ, Zhao YL. Applications of light-responsive systems for cancer theranostics. ACS Appl Mater Interfaces 2018;10(25):21021–34.
[24] Liu R, Yu MN, Yang XT, Umeshappa CS, Hu C, et al. Linear chimeric triblock molecules self-assembled micelles with controllably transformable property to enhance tumor retention for chemo-photodynamic therapy of breast cancer. Adv Funct Mater 2019;29:1808462.
[25] Hu C, He XQ, Chen YX, Yang XT, Qin L, Lei T, et al. Metformin mediated PD-L1 downregulation in combination with photodynamic-immunotherapy for treatment of breast cancer. Adv Funct Mater 2021;31(11):2007149.
[26] Qin Y, Tong F, Zhang W, Zhou Y, He SQ, Xie R, et al. Self-delivered supramolecular nanomedicine with transformable shape for ferrocene-amplified photodynamic therapy of breast cancer and bone metastases. Adv Funct Mater 2021;31(42):2104645.
[27] Hu C, Gao HL. A cleavable self-delivery nanoparticle for tumor photo-immunotherapy. Asian J Pharm Sci 2021;16(2):133–5.
[28] Yu L, Wang Z, Mo Z, Zou B, Yang Y, Sun R, et al. Synergetic delivery of triptolide and Ce6 with light-activatable liposomes for efficient hepatocellular carcinoma therapy. Acta Pharm Sin B 2021;11(7):2004–15.
[29] Yu WQ, Shevtsov M, Chen XC, Gao HL. Advances in aggregatable nanoparticles for tumor-targeted drug delivery. Chinese Chemical Letters 2020;31(6):1366–74.
[30] Gou S, Yang J, Ma Y, Zhang X, Zu M, Kang T, et al. Multi-responsive nanococktails with programmable targeting capacity for imaging-guided mitochondrial phototherapy combined with chemotherapy. J Control Release 2020;327:371–83.
[31] Xie ZJ, Fan TJ, An J, Choi W, Duo YH, Ge YQ, et al. Emerging combination strategies with phototherapy in cancer nanomedicine. Chem Soc Rev 2020;49(22):8065–87.
[32] Siafaka PI, Okur NU, Karantas ID, Okur ME, Gundogdu EA. Current update on nanoplatforms as therapeutic and diagnostic tools: a review for the materials used as nanotheranostics and imaging modalities. Asian J Pharm Sc 2021;16(1):24–46.
[33] Zhou Y, Chen XC, Cao J, Gao HL, et al. Overcoming the biological barriers in the tumor microenvironment for improving drug delivery and efficacy. J Mater Chem B 2020;8:6765–81.
[34] Zhang JM, Li JJ, Shi Z, Yang Y, Xie X, Lee SMY, et al. pH-sensitive polymeric nanoparticles for co-delivery of doxorubicin and curcumin to treat cancer via enhanced pro-apoptotic and anti-angiogenic activities. Acta Biomater 2017;58:349–64.
[35] Zhang JM, Chen R, Fang XF, Chen FQ, Wang YT, Chen MW. Nucleolin targeting AS1411 aptamer modified pH-sensitive micelles for enhanced delivery and antitumor efficacy of paclitaxel. Nano Res 2015;8(1):201–18.
[36] Shi JF, Ren YL, Ma JQ, Luo X, Li JJ, Wu YH, et al. Novel CD44-targeting and pH/redox-dual-stimuli-responsive core-shell nanoparticles loading triptolide combats breast cancer growth and lung metastasis. J Nanobiotechnology 2021;19(1):188.
[37] Owen SC, Chan DPY, Shoichet MS. Polymeric micelle stability. Nano Today 2012;7(1):53–65.
[38] Lu Y, Zhang ES, Yang JH, Cao ZQ. Strategies to improve micelle stability for drug delivery. Nano Res 2018;11(10):4985–98.
[39] Chen XH, Gao HQ, Deng YY, Jin Q, Ji J, Ding D. Supramolecular aggregation-induced emission nanodots with programmed tumor microenvironment responsiveness for image-guided orthotopic pancreatic cancer therapy. ACS Nano 2020;14(4):5121–34.
[40] Qiu YY, Song B, Pezzato C, Shen DK, Liu WQ, Zhang L, et al. A precise polyrotaxane synthesizer. Science 2020;368(6496):1247–53.
[41] Qin L, Cao J, Shao K, Tong F, Yang ZH, Lei T, et al. A tumor-to-lymph procedure navigated versatile gel system for combinatorial therapy against tumor recurrence and metastasis. Sci Adv 2020;6(36):eabb3116.
[42] Stoffelen C, Voskuhl J, Jonkheijm P, Huskens J. Dual stimuli-responsive self-assembled supramolecular nanoparticles. Angew Chem Int Ed Engl 2014;53(13):3400–4.
[43] Song W, Tang Z, Li M, Lv S, Yu H, Ma L, et al. Tunable pH-sensitive poly (beta-amino ester)s synthesized from primary amines and diacrylates for intracellular drug delivery. Macromol Biosci 2012;12(10):1375–83.
[44] Kim J, Shamul JG, Shah SR, Shin A, Lee BJ, et al. Verteporfin-loaded poly(ethylene glycol)-poly(beta-amino ester)-poly(ethylene glycol) triblock micelles for cancer therapy. Biomacromolecules 2018;19(8):3361–70.
[45] Huang Y, Xiao Z, Guan Z, Shen Y, Jiang Y, Xu X, et al. A light-triggered self-reinforced nanoagent for targeted chemo-photodynamic therapy of breast cancer bone metastases via ER stress and mitochondria mediated apoptotic pathways. J Control Release 2020;319:119–34.
[46] Kumari P, Rompicharla SVK, Bhatt H, Ghosh B, Biswas S. Development of chlorin e6-conjugated poly(ethylene glycol)-poly(D,L-lactide) nanoparticles for photodynamic therapy. Nanomedicine 2019;14(7):819–34.
[47] Liang H, Zhou Z, Luo R, Sang M, Liu B, Sun M, et al. Tumor-specific activated photodynamic therapy with an oxidation-regulated strategy for enhancing anti-tumor efficacy. Theranostics 2018;8(18):5059–71.
[48] Li JJ, Wu YH, Wang D, Zou L, Fu CM, Zhang J, et al. Oridonin synergistically enhances the anti-tumor efficacy of doxorubicin against aggressive breast cancer via pro-apoptotic and anti-angiogenic effects. Pharmacol Res 2019;146:04313.
[49] Zou L, Liu XW, Li JJ, Li W, Zhang LL, Fu CM, et al. Redox-sensitive carrier-free nanoparticles self-assembled by disulfide-linked paclitaxel-tetramethylpyrazine conjugate for combination cancer chemotherapy. Theranostics 2021;11(9):4171–86.
[50] Luo YY, Li JJ, Hu YC, Gao F, Leung GPH, Geng FN, et al. Injectable thermo-responsive nano-hydrogel loading triptolide for the anti-breast cancer enhancement via localized treatment based on "two strikes" effects. Acta Pharm Sin B 2020;10(11):2227–45.